Improving the performance of aeroacoustic measurements beneath a turbulent boundary layer in a wake flow

Stefan Haxter * and Carsten Spehr†
German Aerospace Center DLR, D-37073 Göttingen, Germany

Hartmann, M. ‡ Ocker, J. § Tokuno, H. ¶ Wickern,G. ‖

I. Introduction

Experimental measurement and subsequent numerical prediction of the excitation of flat plates or car windows beneath a turbulent boundary layer have become important for the development of novel cars and airplanes. A wavenumber spectrum can be used to define the load on a plat caused by the pressure fluctuations on the surface. Wavenumber spectra from measurements are used to validate the numerical predictions of the acoustic and hydrodynamic portions of the pressure fluctuations. When measuring wavenumber spectra, the design of the experiment can have a large influence on the outcome. In this paper, the effects of both array design and the application of deconvolution algorithms on the experimental determination of the wavenumber-frequency spectrum are evaluated.

The pressure load on a surface beneath a flow can consist of contributions from several characteristic source mechanisms, as summarized by Bremner:[1] first, pressure fluctuations caused by the eddies in a turbulent boundary layer in the flow above the surface; secondly the distinct acoustic pressure field, caused, for instance, by a side mirror in the flow field; and third and fourth, a diffuse acoustic sound field and a broadband rise in the amplitude in the wavenumber domain due to spatially and temporally random events, referred to generally as "rain-on-the-roof" loading.

The importance of each source mechanism depends on the scenario under consideration. In a flight test scenario, the hydrodynamic pressure fluctuations are of importance, since the convective speed of the turbulent eddies in the boundary layer is in the vicinity of the natural oscillation of the fuselage panel. The frequency of this aerodynamic coincidence is nearly the same as the acoustic coincidence on the inner side of the panel facing the cabin. Therefore, the fluctuation energy can be transported efficiently from outside to inside of the cabin. In an automotive scenario, the convective velocity of the eddies is somewhat lower, so that the excitation of a side window by this mechanism is less efficient. The response of a plate to the fluctuating acoustical pressure field comes to the fore. For the numerical prediction of aeroacoustic excitation of a surface, the proportion of energy introduced by each of the mechanisms is of importance. The determination of the contribution of these various energy sources is the aim of many experimental studies, which can themselves then be used to validate the numerical simulations.

Several authors have successfully measured the time-averaged pressure wavenumber-frequency spectrum below a turbulent boundary layer. Arguillat et. al.[2,3] used a rotational array to increase the number of

*PhD student, Institute of Aerodynamics and Flow Technology - Experimental Methods, stefan.haxter@dlr.de
†Research Engineer, Institute of Aerodynamics and Flow Technology - Experimental Methods, carsten.spehr@dlr.de
‡Volkswagen AG, Letterbox 1777, D-38436 Wolfsburg, Germany
§Dr.-Ing. h.c. F. Porsche AG, D-71287 Weissach, Germany
¶Daimler AG, D-71059 Sindelfingen, Germany
‖Audi AG, D-85045, Ingolstadt, Germany

measurement points for the determination of the spectrum. Grulier et al.[4] used a spatio-modal filtering technique on data from a linear array to suppress the signal at wavenumbers related to convection.

Gabriel et al.[5] used a small-sized array with high spatial resolution to obtain flow information at different positions of a generic car model side window. The whole array was moved to measure at different positions on the window and the results were used with the help of triangulation to locate the distinct acoustic source location on the side mirror at approximately 2 kHz.

Ehrenfried & Koop[6] measured the wavenumber spectra in the wind tunnel at flight relevant Mach numbers and applied a deconvolution algorithm to the spectra in order to quantify the energy of each source mechanism. Haxter & Spehr[7,8] performed in-flight measurements on an Airbus model A320 airplane with a similar array design and evaluation.

In the present paper, two measurements with different arrays performed by a consortium of German automotive manufacturers are evaluated. The two measurements were performed with just a different array installed. The aim is to compare the performance of optimized array design to advanced signal processing techniques in terms of deconvolution algorithms. Two measurement points were taken for each array: In a first step, a test case of a generic car model with a side mirror containing a loudspeaker was considered. The aim is to find a known distinct acoustic source beneath the hydrodynamic pressure field of the boundary layer. In a second step, the loudspeaker was switched off and the analysis was performed on the bare flow field with its characteristic acoustics. Each analysis is performed once without deconvolution and once without deconvolution procedures in order to estimate the benefit of this analysis step.

II. Data Processing

A. Wavenumber decomposition

A wavenumber analysis was conducted on the signals of the transducer array.[9] For this, first the discrete cross-spectral density between each of the transducer signals was estimated by performing a temporally averaged Fourier Transform routine by Welch[10] on the data. A window size of 4096 samples was used with an overlap factor of 0.5 and a von Hann window function. The measurement length of 30 s at a sampling frequency of $F_s = 48\,\mathrm{kHz}$ resulted in a total number of $N = 1405$ averages for each cross-spectrum $R[\xi, \eta, f_n]$ at the transducer distances ξ_{gh} and η_{gh} (g and h are the indices of the transducers in the current combination). In equation (1), i represents the current evaluation window index. j represents the square root of -1 with $j = \sqrt{-1}$. In equation (1), t_n is the time index running over the length of the window. The normalized frequency of the corresponding wave is given as a fraction of the window length: $\tilde{f_n}/L$, where $\tilde{f_n} = 0 \ldots L-1$ is the index of the frequency in the frequency vector. The discrete frequencies after transformation are given by $f_n = \tilde{f_n}/L \cdot F_s$. The Fourier Transform of the pressure fluctuations from the time domain to the frequency domain is given by correlating each pressure value $p(t_n)$ with a complex exponential at position t_n:

$$P[\tilde{f_n}]_{g,i} = \frac{1}{L} \sum_{t_n=0}^{L-1} p[t_n]_{g,i} W[t_n] e^{-j\, t_n\, 2\pi \tilde{f_n}/L} \tag{1}$$

The window function W is a weighted Hann window.

$$R\left[\xi_{gh}, \eta_{gh}, f_n\right] = \frac{1}{N} \sum_{i=1}^{N} P_{g,i}\left[f_n\right] P_{h,i}\left[f_n\right]^* \tag{2}$$

The discrete wavenumber analysis is given by:

$$b_{gh}\left[k_x, k_y, f_n\right] = \sum_{g=1}^{M} \sum_{n=1}^{M} R\left[\xi_{gh}, \eta_{gh}, f_n\right] \cdot \exp(-2\pi j \cdot (k_x \xi_{gh} + k_y \eta_{gh})); \tag{3}$$

The calculation of the wave number spectrum is performed as a beamforming algorithm via:

$$b_{gh}\left[k_x, k_y, f_n\right] = \frac{\underline{s}^H_{(k_x,k_y)} R\left[\xi_{gh}, \eta_{gh}, \omega\right] \underline{s}_{(k_x,k_y)}}{\tilde{N}}; \tag{4}$$

where $\underline{s}_{(k_x,k_y)}$ is the steering vector for a planar wave at the position (k_x, k_y) in the steering map given by

$$\underline{s}_{(k_x,k_y)} = \exp(-2\pi j \left(k_x \cdot \underline{x} + k_y \cdot \underline{y}\right)) \tag{5}$$

$\tilde{N}$ is the number of transducer combinations used in the calculation and $(\underline{s})^H$ is the hermite form of $\underline{s}$. The vectors $\underline{x}$ and $\underline{y}$ contain the positions of the sensors during the measurement. Diagonal removal was applied to the cross-correlation matrix. This resulted partly in correlation results with negative value, which were set to zero for deconvolution and machine accuracy ($\approx 2 \times 10^{-16}$). The number of transducer combinations used for correlation was $\tilde{N} = N^2 - N$ with N being the number of transducers. The calculation of the beamforming maps is conducted for a steering map of the size $-25\,\mathrm{m}^{-1} <= k_x <= 75\,\mathrm{m}^{-1}$ with $n_{kx} = 2^8$ points and $-10\,\mathrm{m}^{-1} <= k_y <= 10\,\mathrm{m}^{-1}$ with $n_{ky} = 2^7$ points. This resulted in a two-dimensional plane for each evaluation frequency. Two approaches were used for the display of the data. In the first approach, a slice through the (k_x, k_y)-plane at $k_y = 0$ was extracted for each frequency line and combined as a (k_x, f_n)-diagram. The wavenumbers k_x and k_y are of unit [cycles per length] and not to be confused with the angular wavenumbers of unit [radians per length].

B. Deconvolution

In order to remove the influence of the array-specific point spread function in the beamforming "dirty map", deconvolution algorithms are used to obtain the underlying source map from the experimental beamforming data. The DAMAS2[11] and the CLEAN-SC algorithm[12] was used. A high-wavenumber filter of $k_c = 50/2\pi\,\mathrm{m}^{-1}$, was used for the DAMAS2-algorithm and the filter options were adopted from Ehrenfried & Koop.[13] A gaussian filter function $\phi\left(\hat{k}_x, \hat{k}_y\right)$ was used for the filter:

$$\phi\left(\hat{k}_x, \hat{k}_y\right) = \exp\left(-ln\left(2\right)\right) \frac{\left(\hat{k}_x^2 + \hat{k}_y^2\right)}{k_c^2} \tag{6}$$

For the application of the filter, the mean of the asymmetrically chosen wavenumber map (k_x was chosen to run from $-25\,\mathrm{m}^{-1}$ to $75\,\mathrm{m}^{-1}$), the mean of the extend of this domain was subtracted. The values $\hat{k}_x = k_x - \bar{k_x}$ and $\hat{k}_y = k_y - \bar{k_y}$ were used for the filter setup. In each DAMAS2-iteration, the filter is applied to the two-dimensional Fourier Transform of the source map when convolving the source map with the point-spread-function.

For the iterative solution of the deconvolution problem, the wavenumber domain was zero-padded by one length of the domain in both positive and negative k_x and k_y-direction. The point spread function was calculated for the entire domain in order to ensure that the effects of souces that were possibly located at the outskirt of the source map had an effect on the entire map when convolved with the point spread function. This resulted in a more stable execution of the DAMAS2-algorithm. A total number of 5000 iteration cycles were conducted.

The application of the deconvolution algorithms was expected to drastically narrow the main lobe width. Since it was possible for acoustic sources to appear slightly off the center of the two-dimensional wavenumber spectrum in which the deconvolution took place, the slice which was extracted for plotting at $k_y = 0$ was broadened and the mean value was taken. The slice was extended from a width of one gridpoint to a width of three grid points which corresponded to $k_y = 0 \pm 1\,\mathrm{m}^{-1}$.

C. Separation of Pressure Spectra

After deconvolution, the acoustic part of the two-dimensional (k_x, k_y)-planes were separated via

$$(k_{x,acoust.}, k_{y,acoust.}) = k_0 \left(\frac{\cos\theta}{1 + M\cos\theta}, \frac{\sin\theta}{1 + M\cos\theta}\right). \tag{7}$$

In equation (7), M is the Mach number, k_0 is the wavenumber of waves propagating at the speed of sound and θ is the angle from the origin in the wavenumber domain. All waves appearing within the ellipse $(k_{x,acoust.}, k_{y,acoust.})$ are of acoustic nature. All waves outside this ellipse are of convective nature. The integral value over each of the regions represents the power spectral density (PSD) induced by that particular propagation characteristic.

III. Preliminary experiments[a]

A. Experimental Setup

The setup was the same for the measurement with each array: A generic vehicle model based on the SAE Type 4 (fullback) was used for testing. A summary of the experimental setup, a first evaluation of the preliminary experiment, and a comparison with numerical data are given in the original paper.[14] On the left hand side, a generic driver window was cut from the body and was replaced by a measurement window. This window was made of high-density foam and equipped with flush-mounted half-inch surface microphones of type Brüel and Kjær 4949. The distribution of the microphones on the window in the first test is shown in figure 1. The positions extend throughout the whole window. In the lower right part of the array an equidistant distribution in x- and y- direction was selected, which allows a straightforward and fast calculation of a spatial Fourier transform over the array positions. An outline of the transducer positions is also shown in the figure. It gives an indication of the shape of the window.

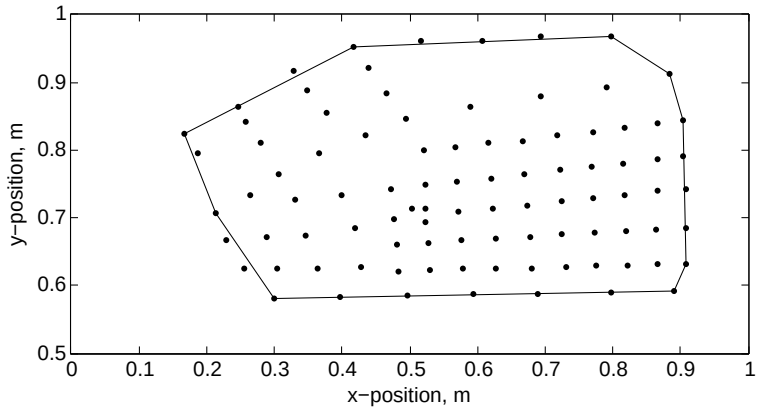

Figure 1. Sketch of the microphone positions behind the side-view mirror

A total of 96 microphones were installed in the window, of which three were positioned in front of the side view mirror. These three microphones are not used in the present evaluation. A sampling frequency of $F_s = 48\,\text{kHz}$ was used. The measurement time was 30 s. Right in front of the array, a side view mirror was attached to the SAE body in order to obtain a flow field characteristic for a generic vehicle. On its downstream side, the mirror contained a loudspeaker that could be used to apply arbitrary acoustic waves on the array. In the frequency range between 300 Hz and 2000 Hz, the loudspeaker delivered a white noise of approximately 88 dB.

B. Selection of window segments for evaluation

For the determination of the appropriate measurement position on the array a map of the root mean-square of the pressure fluctuation was created. The distribution of the magnitude of the pressure fluctuations is shown in figure 2. In the front part, behind the side-view mirror, the pressure fluctuation magnitude is greatest due to the detached flow behind the mirror. In the upper front part of the window, another area of detached flow is visible, this arising from the vortex of the a-pillar. In the lower rear part of the window, an area of nearly constant - i.e. space invariant - pressure fluctuation magnitude can be seen; this region (framed in red) was chosen for evaluation. In order to show the influence on the evaluation of the location

[a]See AIAA 2012-2205 from the 18th AIAA/CEAS Aeroacoustic Conference in reference 14

of measurement and the inhomogeneity of the flow, the front transducers (as framed in red in figure 2) were included in the subset in a separate analysis.

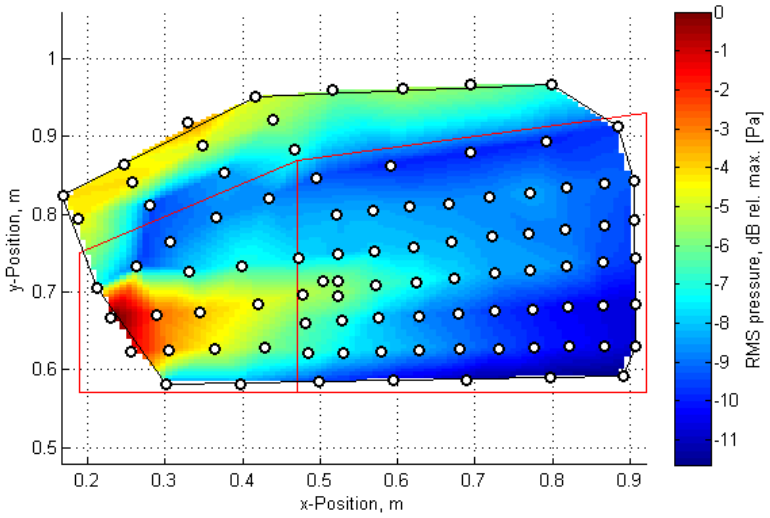

Figure 2. Distribution of pressure RMS on the side window (interpolated, transducer positions shown as black/white dots)

The array properties of each array subset are shown in figure 3. In 3(a), the array positions in the area where the flow is considered to be sufficiently space-invariant are shown. The equidistant setup is clearly visible here. In figure 3 (b), the point-spread function (PSF) of a single planar wave excitation of this subset is displayed. The rectangular pattern of side lobes appearing in the PSF results from aliasing effects caused by the equidistant distribution of the transducers with relatively large spacing in this area. The maximum side lobe level relative to the main lobe is $-3.6\,\mathrm{dB}$ at a position of of $(k_\mathrm{x}, k_\mathrm{y}) \approx \pm(20\,\mathrm{m}^{-1}, 2\,\mathrm{m}^{-1})$. Figure 3 (c) shows the transducer distribution with the elements directly behind the side-view mirror included in the subarray. The resulting point-spread-function is shown in figure 3 (d). The rectangular side lobe distribution is still visible and the side lobes appear at the same positions as when only the aft subset is evaluated. However, the amplitude of the side lobes has decreased to $-5.1\,\mathrm{dB}$ at $(k_\mathrm{x}, k_\mathrm{y}) \approx \pm(2\,\mathrm{m}^{-1}, -19\,\mathrm{m}^{-1})$ due to the increased number of transducer positions outside of the rectangular grid.

C. Results

In the following, the results from the measurements using the preliminary array are shown. The real-part of the results are plotted in the wavenumber-frequency domain and are normalized to the maximum in each particular map.

Before going into detail about the frequency region below 2 kHz, at first a brief look is taken up to a frequency of 10 kHz in figure 4 for the case with the loudspeaker in the side mirror switched on. The aft subarray was used for evaluation. The amplitudes in the figure are plotted in dB relative to the maximum value in the map. An acoustic signal is clearly visible extending at a steep angle from the origin. What is also visible are the side lobes which result from the spatial aliasing of the pressure fluctuations. If this is known, however, it is possible to identify the correct main lobe (the one going through the origin) and detect the acoustic signal down to frequencies as low as approximately 1 kHz.

One region of interest is, however, the frequency region where the convective ridge is visible and the most dominant part in the plot. The convective ridge is visible in red in the lower part of figure 4 at a flat angle compared to the acoustic signal. In this region, the acoustic domain is covered by the side lobes of the convective ridge, which makes an identification of the acoustic signal difficult. In the further discussion, the focus is set on the frequency region from 0 Hz to 2 kHz.

Figures 5 displays the wavenumber-frequency-plots from the larger subarray shown in figure 3. The measurements were obtained at a speed of 140 km/h with the loudspeaker in the side mirror switched on. The main lobe of the convective ridge is seen to extend from the origin of the wavenumber-frequency domain

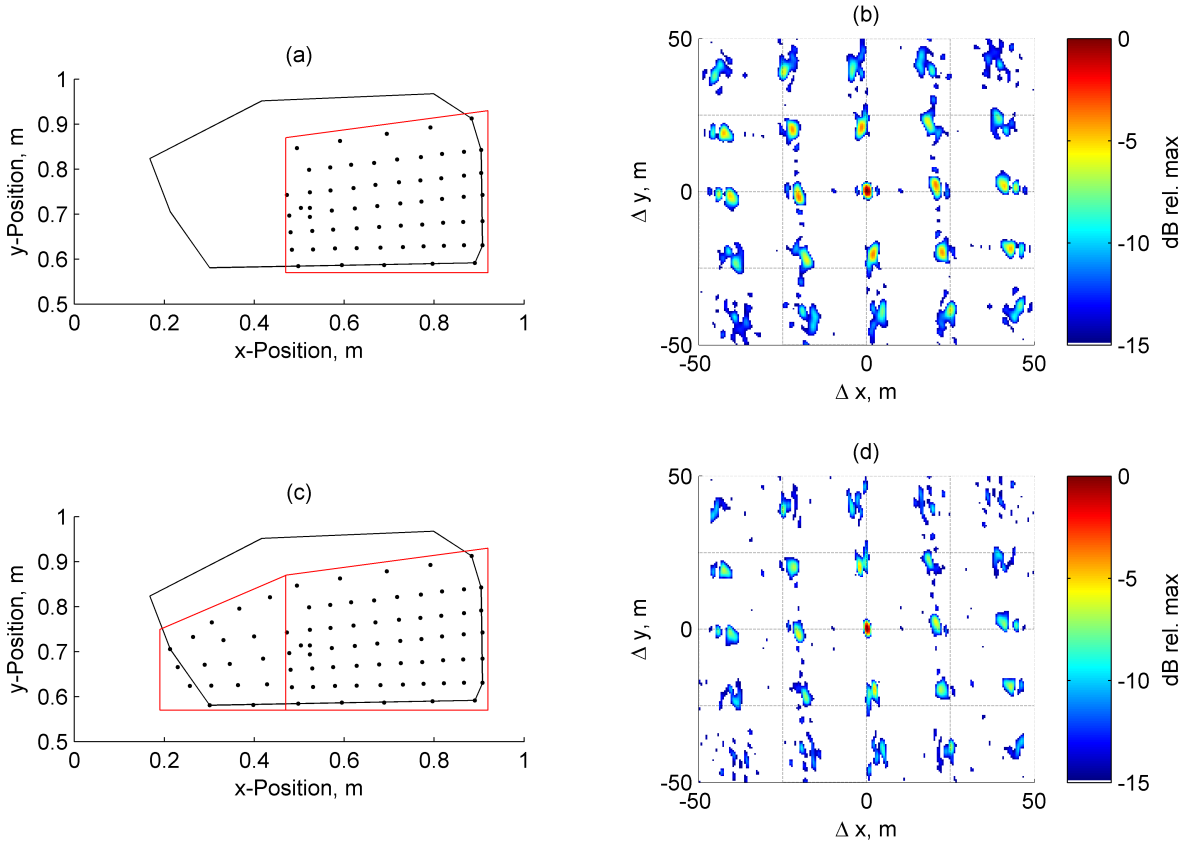

Figure 3. Subarrays of the total number of transducers (left) and their point-spread-function (right): (a)+(b) back part; (c)+(d) back and front part

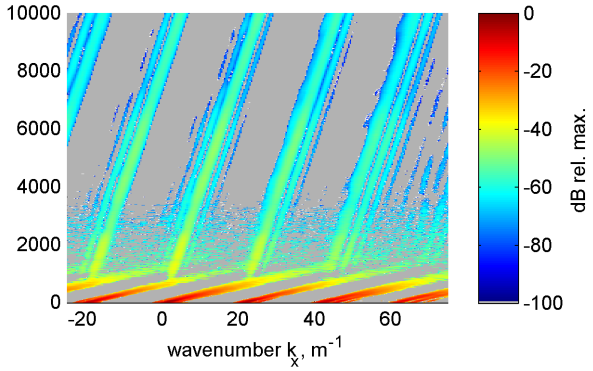

Figure 4. Evaluation of the initial aft-array up to a frequency of 10 kHz at 140km/h; Loudspeaker switched on

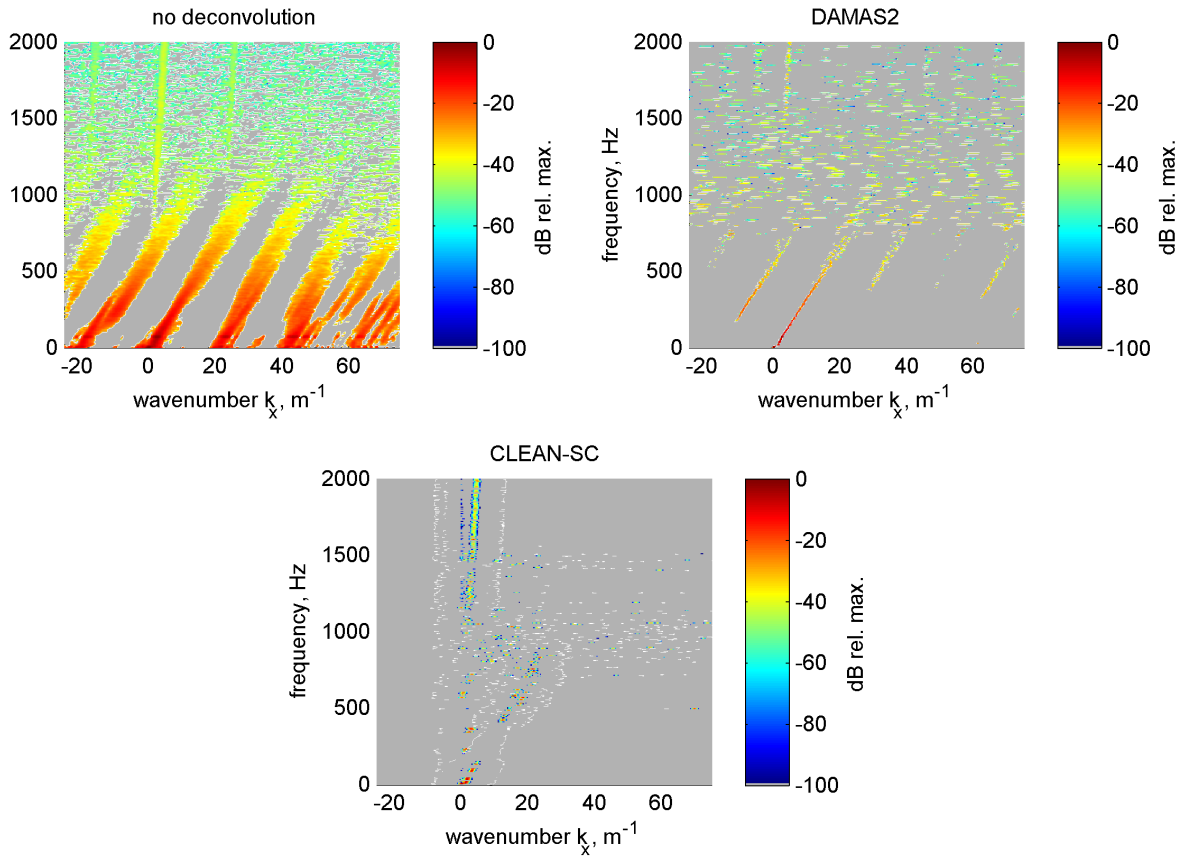

Figure 5. Wavenumber-frequency diagram using with selected microphone positions: front+back; Loudspeaker in side mirror on; 140 km/h (a) no deconvolution; (b) DAMAS2; (c) CLEAN-SC

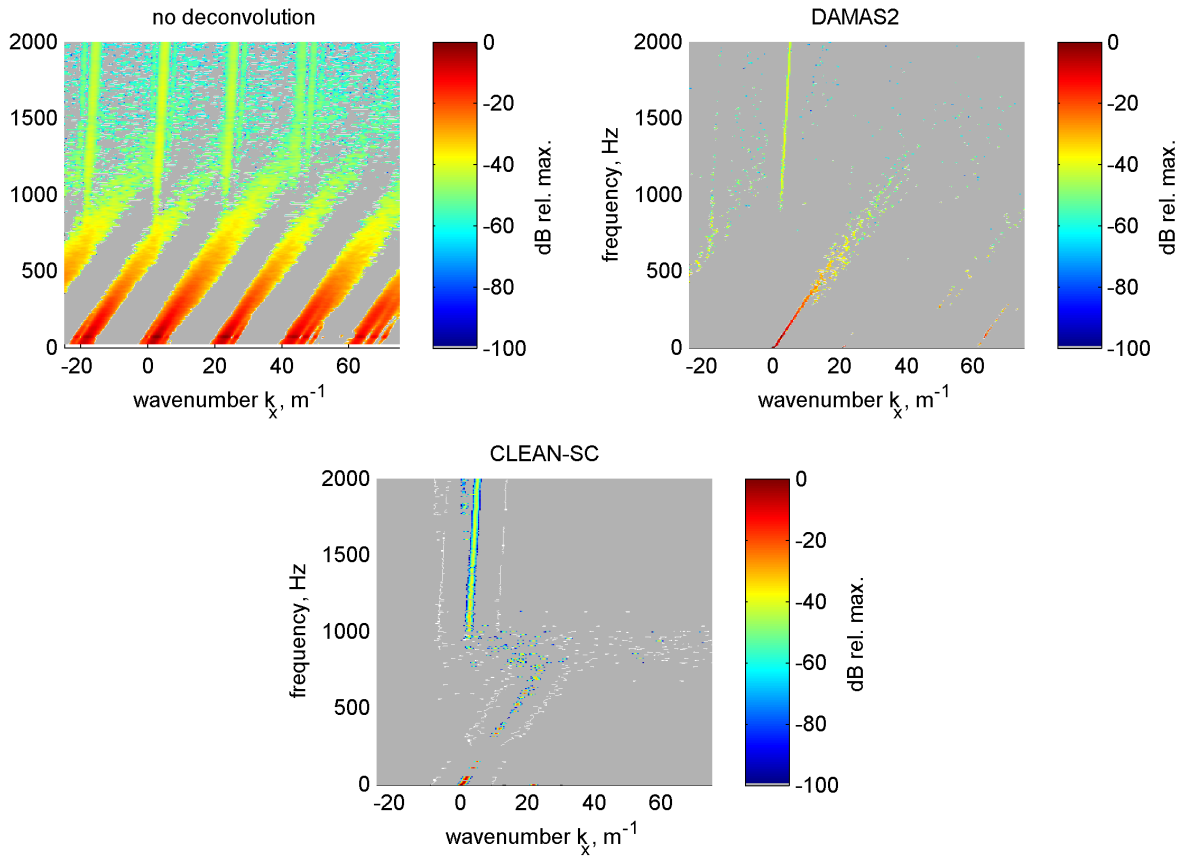

Figure 6. Wavenumber-frequency diagram using with selected microphone positions: back; Loudspeaker in side mirror on; 140 km/h (a) no deconvolution; (b) DAMAS2; (c) CLEAN-SC

at $(\omega = 0, k_x = 0)$. Several very similar side lobes of this main lobe are visible at multiples of $k_x \approx \pm 20\,\mathrm{m}^{-1}$, as shown in the plots of the array pattern in figure 3. The convective ridge is a dominant feature of the wavenumber-frequency plot up to a frequency of approximately 1.1 kHz. From here on, an acoustic wave is visible in extention of the origin at a steeper angle than the convective ridge. This acoustic wave is overlain by a side lobe of the convective ridge in the frequency range from 1.1 kHz up to 1.5 kHz. Above this frequency, the acoustic pressure fluctuations are the prominent feature in the wavenumber frequency spectrum. Deconvolution using the DAMAS2 algorithm enhances the main lobe and reduces the side lobes drastically. The main lobe is sharpened and instead of a broad main lobe appears as a single line. Below 100 Hz, the algorithm removes all the side lobes. With increasing frequency, the several side lobes are visible which however, are reduced from former side lobe width to a single line as well. Above 800 Hz, the deconvolved source map starts to blur and neither convective ridge, nor an acoustic signal are visible. Above 1500 Hz, an acoustical signal can be slightly seen.

Deconvolution using the CLEAN-SC algorithm is shown in the lower part of figure 5. This algorithm is not able to identify the acoustic part of the spectrum well, since this part is not the prominent feature of the map. Rather, a large number of small distributed sources is seen above a frequency where the convective ridge is not the dominant feature of the plot any more. The identification of the convective ridge by the CLEAN-SC algorithm shows gaps at many frequencies. Yet, the inclination of the convective ridge is slightly visible. The application of CLEAN-SC was performed in the two-dimensional wavenumber domain, each frequency at a time. Since the sources are located at the positions of the maximum in the wavenumber domain and are represented by Gaussian plots, the position of the maxima at the gap positions might be off the $k_y = 0$-centerline at which the slice through the wavenumber domain was taken, as depicted.

In figure 6, the results of the evaluation using only the rear part of the array are shown. The same features of the pressure fluctuations as in the larger subarray are observed. The acoustic wave propagation is however, more prominent and can be identified down to a frequency as low as 900 Hz. Sidelobes are visible for both, the convective ridge and the acoustic waves. Especially for the acoustic waves, the side lobes are more prominent, which is caused by the more equi-distant spacing of the microphones in the smaller subarray. The DAMAS2 algorithm removes the side lobes almost completely and reduces the main lobes to a narrow line. This works best for the convective ridge at low frequency up to 400 Hzand the acoustic signal, which is visible above 1000 Hz. In between, the algorithm is not able to resolve the broadening of the convective ridge due to spatial de-correlation of the turbulent boundary layer pressure fluctuations. Above 1000 Hz, the acoustic signal is the dominant feature in the spectrum.

The CLEAN-SC algorithm is able to identify the acoustic waves down to a frequency of approximately 1 kHz. Above this frequency, it is able to remove all the sidelobes from the map. Below, the hydrodynamic component is too distinct. It should be mentioned that the CLEAN-SC algorithm was developed to remove dominant acoustic sources from measurements in order to increase the signal-to-noise ratio of the evaluation process. The reason, why the acoustic pressure fluctuation is not found underneath the dominant hydrodynamic pressure fluctuation is, that the hydrodynamic pressure fluctuations are spatially de-correlated, as described by the Corcos model,[15] or the Efimtsov model.[16] This de-correllation is not resolved by the CLEAN-SC algorithm which is therefore not applicable to entirely remove spatially de-correlated sources.

The comparison of the two subarrays illustrates the relevance of the array position in the vicinity of strong wake fluctuations: in the case under consideration, the evaluation of a smaller array with less sensors is more suitable than a larger array in order to distinguish between acoustic and hydrodynamic fluctuations.

Figure 7 displays the results from the larger subarray at the speed of 140 km/h but with the loudspeaker in the side mirror off. The convective results shows only a convective ridge and the side lobes. Noo acoustic waves are visible. The application of the CLEAN-SC algorithm does not improve the result.

- hier

In figure 8, the same measurement is shown, but with only the microphones in the small aft subarray were used for evaluation. The convective ridge is still the most dominant part in the figure, but in contrast to the evaluation with the larger subarray, an acoustic signal is seen, which is however superimposed by a side lobe of the convective ridge. The application of the DAMAS2 removes most of the side lobes and the acoustic signal above 1200 Hz is exposed from underneath a side lobe from the convective ridge. The CLEAN-SC algorithm is not able to identify acoustic sources underneath the hydrodynamic sources. This is again caused by the non-prominence of the acoustic waves which are not identified by the algorithm as a result. Again, a smaller array with less elements is able to produce results which a larger area cannot. This once more shows the significance of accurate selection of the measurement area as also shown by Gabriel.[5]

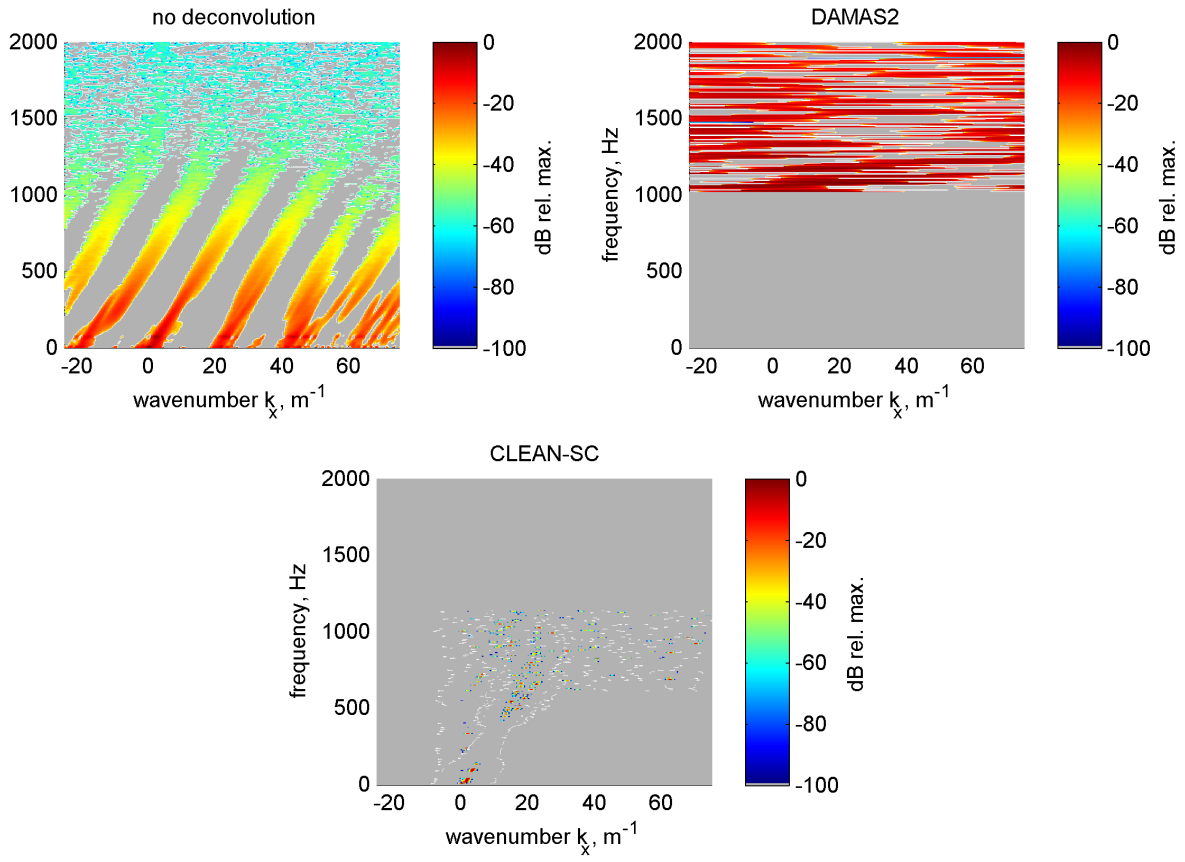

Figure 7. Wavenumber-frequency diagram using with selected microphone positions: front+back; Loudspeaker in side mirror off; 140 km/h; (a) no deconvolution; (b) DAMAS2; (c) CLEAN-SC

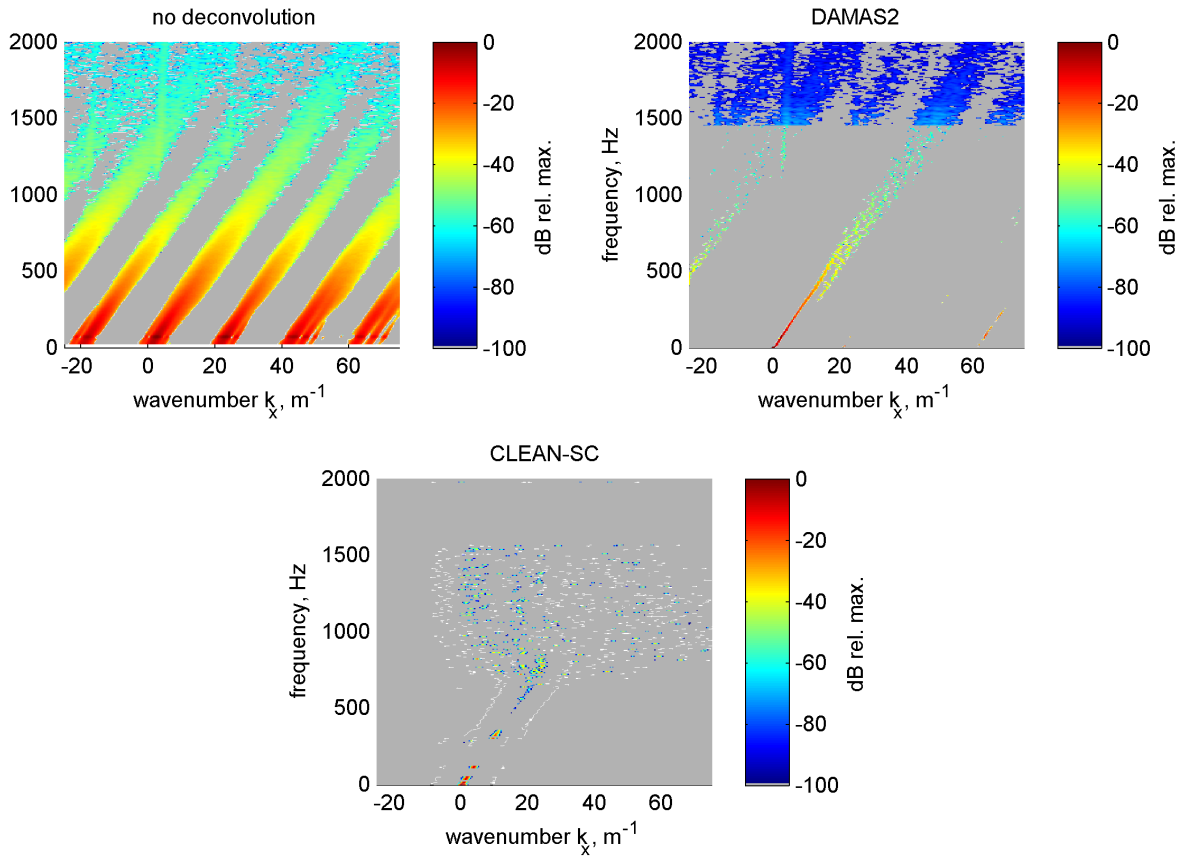

Figure 8. Wavenumber-frequency diagram using with selected microphone positions: back; Loudspeaker in side mirror off; 140 km/h; (a) no deconvolution; (b) DAMAS2; (c) CLEAN-SC

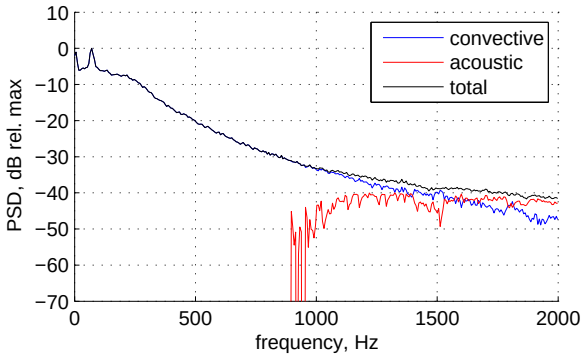

Figure 9. Separated Pressure Spectra with Loudspeaker on; preliminary array; DAMAS2 algorithm applied to WFS; aft subarray

In figure 9, the separated spectra of the acoustic and hydrodynamic pressure fluctuations are shown for the case with the loudspeaker in the side mirror switched on. The amplitudes were normalized to the maximum value in the spectrum. The acoustic pressure fluctuations can be seen above a frequency of 900 Hz. The level raises up to a frequency of 1100 Hz from where it stays constant. The level of the hydrodynamic pressure fluctuations drop with frequency and drops below the acoustic level above 1500 Hz. Below 900 Hz, no acoustic level is identified. The maximum difference in level between the acoustic and the hydrodynamic spectrum is approximately 18 dB at a frequency of 900 Hz.

D. Interim conclusion

The first measurement campaign successfully shows the possibility of an experimental separation between acoustic and hydrodynamic pressure fluctuations. The right choice of evaluation area reveals a significant difference in the obtained results. Even the evaluation with less sensors can significantly improve the results.

Regarding equation (3) it appears that the wavenumber decomposition can be seen as a two-dimensional Fourier transformation. The pressure fluctuation measurements were sampled spatially with an irregular pattern so that the Fast Fourier algorithm cannot be applied. Nevertheless the wavenumber decomposition tries to represent the whole datasample within the evaluation window as a set of complex exponential functions. The wake development behind the side mirror causes different wavelengths in different areas of the evaluation window. The representation of such a pressure distribution by complex exponential functions does not provide a discrimination between the different areas and is only possible with additional higher wavenumber content. In other words: the wavenumber decomposition includes a spatial average over the selected range which hinders the discrimination between the different structures. A smaller evaluation segment including a spatially invariant fluctuation range matches the assumptions of a wavenumber decomposition much better, where the algorithm examines the similarity of spatial fluctuation distribution with plane waves of different wavelengths. The application of the DAMAS2 deconvolution algorithm increases the quality of the maps. The main lobe is sharpened and the side lobes are largely removed. In one case, the acoustic signal was uncovered from a side lobe of the dominant convective ridge. The CLEAN-SC algorithm is not able to resolve further acoustic sources underneath the hydrodynamic pressure fluctuations. The reason for this is believed in the non-de-correlation-assumption in the CLEAN-SC algorithm which does not apply to hydrodynamic pressure fluctuation and hinders the algorithm to execute at full potential.

The overlap of the acoustic wavelength with the broad and distinguished side lobes in the relevant frequency range around 1000 Hz provided the impetus for a second measurement campaign with an microphone array distribution optimized for the purpose of this discrimination.

IV. Measurements with optimized array

A. Improvement of the array resolution in the segment of choice

The aim of array design is to increase the ratio of main lobe to side lobes in the point spread function of the array having only a limited number of array elements at hand. The number of unique sensor spacings relative to the maximum number of sensor spacings possible is a good first indicator for the goodness of the array distribution.

The microphone array was optimized for the application of wave number decomposition. A region of interest was defined in which all the microphones had to be located.

A multi-arm spiral array approach with seven arms was used for the distribution of the array elements as described by Underbrink.[17] The inclination of the spiral arms, the inclination of the logarithmic distribution of elements along each arm, and the center point were left for variation. A Genetic Algorithm Toolbox for Matlab[18] was then used to iterate and vary these parameters. As a cost function, the main lobe to side lobe ratio in the wavenumber space was used. This ratio was found by calculating the point spread function of a planar wave excitation on the array on a defined evaluation grid and determining the value for the first side lobe in dB. The lower the first side lobe was found to appear, the better the array distribution was rated. The region of interest, transducer dimension, and the number of transducers used were restrictive elements in the iterative optimization process. Although it was not quantified, the main lobe width was minimized by extending the array elements over the whole space available in order to maximize the aperture size.

The resulting array distribution is shown in figure 10 (a). The center point of the array is clearly visible surrounded circularly by the second elements of the spiral arms.

The resulting point spread function of this distribution is shown in figure 10 (b). The main lobe to side lobe ratio was found to be 10.6 dB at a side lobe position of $(k_x, k_y) \approx \pm(28\,\mathrm{m}^{-1}, 3\,\mathrm{m}^{-1})$. The side lobes have been successfully suppressed by the distribution of the array elements in several logarithmic spirals.

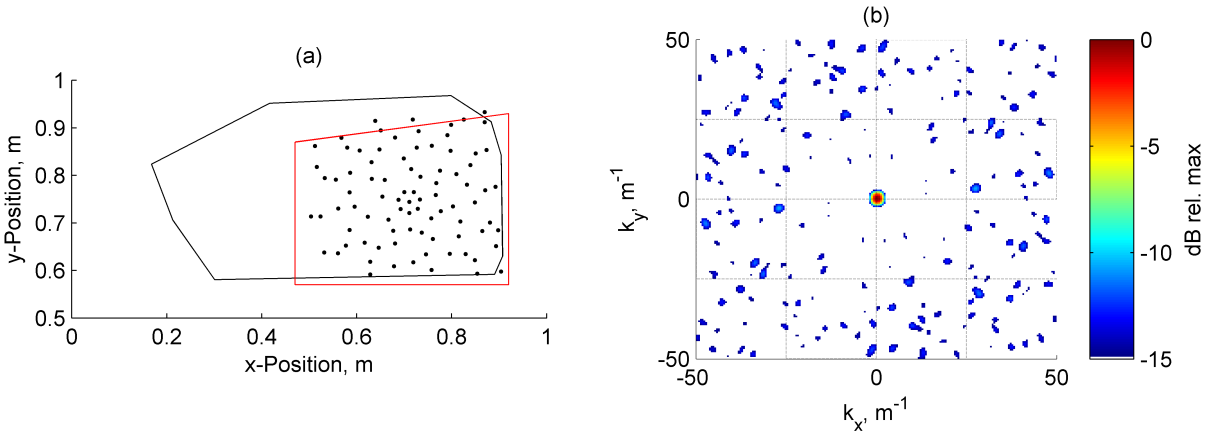

Figure 10. Optimized array: (a) transducer position (with former array region shown as a red surrounding) (b) PSF

B. Experimental Setup

The setup of the second measurement was similar to that of the first, except for the exchange of the array. The array was again installed on the left hand side of the SAE body. As before, a side-view mirror had been attached right in front of the array, and it also was equipped with a loudspeaker on its downstream side.

C. Results

In the following, the results from the measurements using the optimized array are shown. The results are again plotted in the wavenumber-frequency domain and are again normalized to the maximum in each particular map. Again, at first, the frequency range up to 10 kHz is shown in figure 11 with the loudspeaker in the side mirror switched on. The sidelobes are drastically suppressed by the optimized array design. Acoustic pressure fluctuations are detectable very well at high frequencies. In the low-frequency region, the convective ridge is still the dominant feature of the spectrum. However, there are no more sidelobes of the convective ridge that interfere with the acoustic domain. In the following, the focus is again set to the frequency region below 2 kHz.

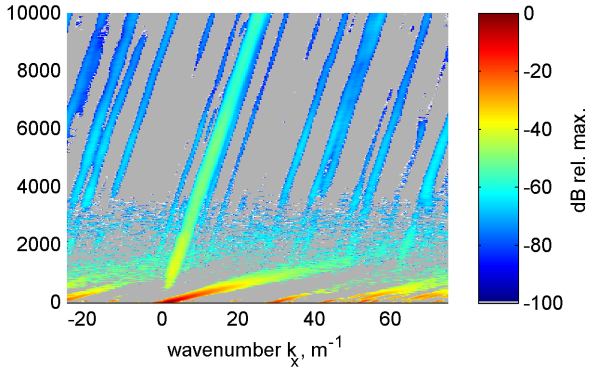

Figure 11. Evaluation using the optimized array up to a frequency of 10 kHz at 140km/h; Loudspeaker switched on

The wavenumber-frequency spectra resulting from the optimized array with the loudspeaker inside the side mirror switched on are shown in the upper left of figure 12. As expected, the side lobes of both, the

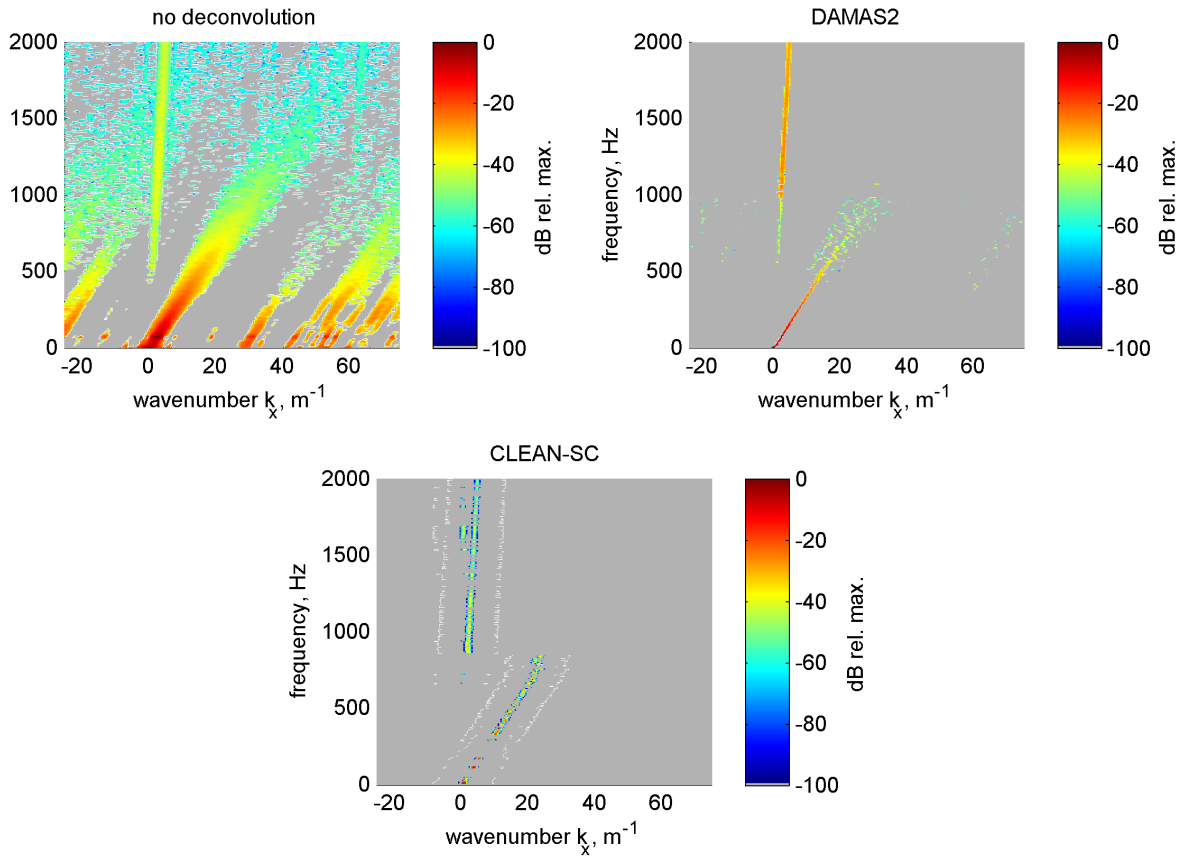

Figure 12. Frequency-wavenumber diagram with optimized sensor position; Loudspeaker on; 140 km/h; (a) no deconvolution; (b) DAMAS2; (c) CLEAN-SC

convective ridge and the acoustic pressure flucutations are drastically removed. The acoustic wavelengths emitted by the loudspeaker are clearly visible down to a frequency of 500Hz with only little interference from a side lobe from the convective ridge. At this frequency of 500 Hz, the PSD of the loudspeaker is approximately 15 dB beneath the PSD of the hydrodynamic fluctuations. The side lobes of the convective ridge interfere much less with the acoustic wavelength than in the case of the initial array, especially in the low wavelength range. The flat frequency slope of the loudspeaker noise signal is visible.

The DAMAS2 deconvolution algorithm removes again the remaining parts of the side lobes and sharpens the main lobe for both, the acoustic and hydrodynamic signal. However, since the acoustic signal is not covered by a distinct side lobe in the case of no deconvolution, no further information is obtained. The acoustic signal shows a flat slope above a frequency of 1000 Hz. From 600 Hz up to 1000 Hz, the level is still constant, but lower. This is caused by the position of the acoustic signal not being at $k_x = 0\,\mathrm{m}^{-1}$ in the wavenumber spectrum, although the speaker is not moved. The reason for this is believed in the co-existence of an acoustic signal and a convective ridge of equal strength, which leads to an imprecise reconstruction of both sources. The CLEAN-SC algorithm is able to identify the acoustic pressure fluctuations down to a frequency of approximately 900 Hz. Below this frequency, the convective ridge is again the dominant feature of the spectrum and the acoustic pressure fluctuations are buried underneath the hydrodynamic pressure fluctuations - unobtainable to the CLEAN-SC algorithm.

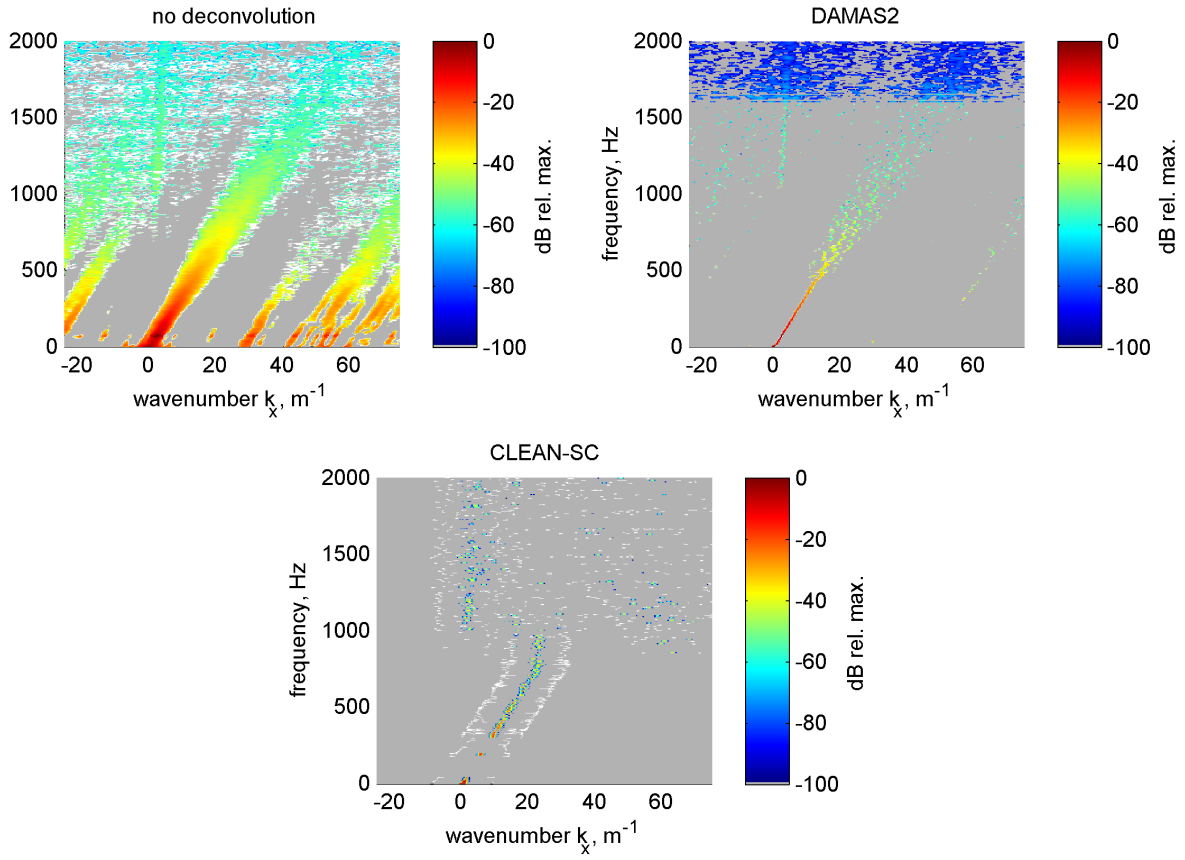

Figure 13. Frequency-wavenumber diagram with optimized sensor position; Loudspeaker off; 140 km/h; (a) no deconvolution; (b) DAMAS2; (c) CLEAN-SC

Figure 13 (a) shows the results at 140 km/h, with loudspeaker off and without deconvolution. The side lobes of the convective ridge are much less pronounced which enhances the identification of an acoustic signal in the frequency range between 1000 Hz and 1200 Hz. Application of the DAMAS2 deconvolution is able to uncover the acoustic signal from underneath the side lobe. This works better than in the case of the initial array, since the side lobe level is lower for the optimized array. An acoustic signal can be identified above 1000 Hz. When using the CLEAN-SC algorithms, the presence of acoustic waves can be seen above 1000 Hz as well. However, the DAMAS2-algorithm delivers a more smooth result of both the convective ridge and

the acoustic signal.

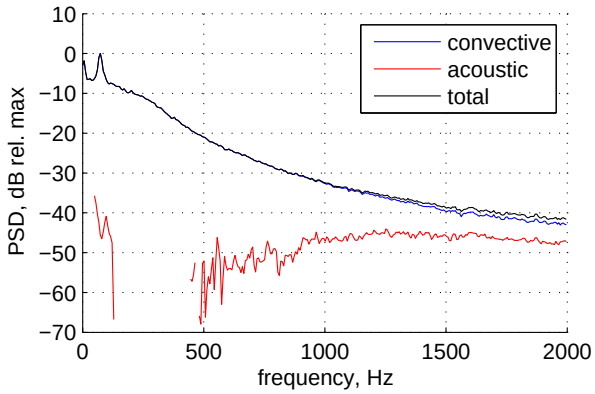

Figure 14. Separated Pressure Spectra with Loudspeaker on; optimized array; DAMAS2 algorithm applied to WFS

- hier

The separately integrated acoustic and convective spectrum is shown for the optimized array in figure 14 for the measurement with the loudspeaker in the side mirror switched on. The acoustic spectrum shows flat "white noise" above a frequency of 1000 Hz. Between 500 Hz and 1000 Hz, the acoustical amplitude is reduced due to the acoustic level being too low to resolve beneath the convective ridge. However, the acoustic portion of the spectrum in this frequency range is not caused by a side lobe. Between 300 Hz and 500 Hz no signal has been detected, due again to the dominance of the convective pressure fluctuations. Below 300 Hz, the signal from the loudspeaker was lowered and dropped with approximately 20 dB per octave. Again, at frequencies below 150 Hz, the power spectral density in the acoustic spectrum is raised due to the main lobe of the convection leaking in the acoustic domain.

V. Conclusion

The distribution of microphones for the array measurement technique can be optimized to place increased emphasis on particular features of interest.

A known acoustical source had been located significantly better with an optimized array than by application of deconvolution algorithms.

In accordance with Gabriel[5] the results show that a small array can give better results in spatially quasi-invariant flow fields than a large array due to the higher spatial resolution. This can even apply, if a small array contains less microphones than a larger one. A small array however increases the width of the main lobe and therefore drastically limits the array resolution at low frequencies and large wavelengths.

Major side lobes were removed from the dirty maps using the DAMAS2 algorithm. This resulted in the uncovering of acoustic signal when it was superimposed by the influence of a distinct side lobe of the convective ridge. The combination of both an optimized array and the application of a deconvolution algorithm showed the best results. In the case of no loudspeaker signal being present, an acoustic signal was identified down to a frequency of 1000 Hz. The CLEAN-SC algorithm was able to identify the dominant feature of the map at each frequency, but the result was less pronounced.

A dynamic range of the wavenumber analysis has been observed: the acoustic waves are not visible if the convective ridge is too dominant. Unfortunately, this is the case in the low-frequency region where an array with a much higher signal-to-noise ratio would be needed in order to resolve acoustical wave propagation at even lower amplitudes underneath the convective ridge. When integrating the acoustic and convective domain separately,

- hier

the side lobes of the convective ridge can distort considerably the amplitude of the acoustic level. An optimized array pattern is considered to have a stronger effect on the resolution than application of the DAMAS2 deconvolution algorithm. The CLEAN-SC algorithm, which works in an essentially different way than the DAMAS2 algorithm has the drawback that the dominant hydrodynamic pressure fluctuations are not represented well by the assumptions of the algorithm.

The combination of using an optimized array and the DAMAS2 deconvolution algorithm showed the best results.

References

[1]Bremner, P. G., "Vibroacoustic Source Mechanisms under Aeroacoustic Loads," *18th AIAA/CEAS Aeroacoustics Conference, Colorado Springs, Colorado*, AIAA, June 2012.

[2]Arguillat, B., Ricot, D., Robert, G., and Bailly, C., "Measurements of the wavenumber-frequency spectrum of wall pressure fluctuations under turbulent flows," *AIAA-2005-2855*, 2005.

[3]Arguillat, B., Ricot, D., Bailly, C., and Robert, G., "Measured wavenumber: Frequency spectrum associated with acoustic and aerodynamic wall pressure fluctuations," *Journal of the Acoustical Society of America*, Vol. 128(4), 2010, pp. 1647–1655.

[4]Grulier, V., Debert, S., Mars, J., and Pachebat, M., "Acoustic and turbulent wavenumbers separation in wall pressure array signals using EMD in spatial domain," *Acoustics, Speech and Signal Processing, 2008. ICASSP 2008. IEEE International Conference on*, 2008, pp. 333–336.

[5]Gabriel, C., Mller, S., Lech, R., and Ullrich, F., "Measurement of the Spatial Coherence of Surface Pressure in the Wake of a Car's Side Mirror," *19th AIAA/CEAS Aeroacoustics Conference, Berlin, Germany*, AIAA, May 2013.

[6]Ehrenfried, K. and Koop, L., "Experimental study of pressure fluctuations beneath a compressible turbulent boundary layer," *AIAA 2008-2800*, 2008.

[7]Haxter, S. and Spehr, C., "Two-Dimensional Evaluation of Turbulent Boundary Layer Pressure Fluctuations at Cruise Flight Condition," *18th AIAA/CEAS Aeroacoustics Conference, Colorado Springs, Colorado*, AIAA, June 2012.

[8]Spehr, C., Hennings, H., Bouhaj, M., Hebler, A., and Buchholz, H., "In-flight sound Measurements: A first overview," *18th AIAA/CEAS Aeroacoustics Conference, Colorado Springs, Colorado*, AIAA, June 2012.

[9]Haxter, S. and Spehr, C., "Infinite Beamforming: Wavenumber Decomposition of Surface Pressure Fluctuations," *Proceedings of the 5th Berlin Beamforming Conference, Berlin, Germany*, February 2014.

[10]Welch, P. D., "The use of fast Fourier transform for the estimation of power spectra: A method based on time averaging over short, modified periodograms," *Audio and Electroacoustics, IEEE Transactions on*, Vol. 15, No. 2, 1967, pp. 70–73.

[11]Dougherty, P., "Extensions of DAMAS and benefits and limitations of deconvolution in beamforming," AIAA, Monterery, CA, May 2005.

[12]Sijtsma, P., "CLEAN based on spatial source coherence," *International Journal of Aeroacoustics*, Vol. 6, 2007, pp. 357–374.

[13]Ehrenfried, K. and Koop, L., "A comparison of iterative deconvolution algorithms for the mapping of acoustic sources," *AIAA Jounal*, Vol. 45, No. 7, 2006, pp. 1584–1595.

[14]Hartmann, M., Ocker, J., Timo, L., Mutzke, A., Schwarz, V., Tokuno, H., Toppinga, R., Unterlechner, P., and Wickern, G., "Wind Noise caused by the A-pillar and the Side Mirror flow of a Generic Vehicle Mod," *18th AIAA/CEAS Aeroacoustics Conference, Colorado Springs, Colorado, USA*, 2012.

[15]Corcos, G. M., "Resolution of Pressure in Turbulence," *The Journal of the Acoustical Society of America*, Vol. 35, No. 2, 1963, pp. 192–199.

[16]Efimtsov, M., "Characteristics of the Field of Turbulent Pressures at the Wall of a Boundary Layer," *Sov. Phys. Acoust.*, Vol. 28, No. 4, 1982, pp. 289–292.

[17]Mueller, T. J., editor, *Aeroacoustic Measurements*, Springer, 2002.

[18]Chipperfield, A., Fleming, P., Pohlheim, H., and Fonseca, C., "Genetic Algorithm TOOLBOX For Use with MATLAB," Tech. rep., 1994.